Received: Added at production | Revised: Added at production | Accepted: Added at production
DOI: xxx/xxxx

ARTICLE TYPE

# Multiphysics Simulation of Recent Experiments on Alkali-Silica Reaction Expansion in Reinforced Concrete Members

Amit Jain | Benjamin W. Spencer | Albert Dahal | Sudipta Biswas | Somayajulu L. N. Dhulipala

[1]Computational Mechanics and Materials, Idaho National Laboratory, P.O. Box 1625, Idaho Falls, Idaho 83415-3840, USA

**Correspondence**
Benjamin W. Spencer, Email: benjamin.spencer@inl.gov

**Summary**

Alkali-silica reaction (ASR) is an important long-term degradation process in concrete structures. ASR produces expansive silica gel, causing local damage and macroscopic expansion, which can lead to cracking and damage throughout a structure due to load redistribution. ASR progression is affected by aggregate reactivity, alkali content in the hardened cement paste, temperature, moisture content, and stress. Numerical simulation is essential to predict the progression and effects of ASR on the performance of structures. Because of the interactions between thermal and moisture transport and mechanical deformation, it is important for numerical models to represent all these physical phenomena and the interactions between them. Simulations of ASR in reinforced concrete (RC) structures are further complicated by the need to capture interactions between concrete and embedded reinforcing bars. This paper describes the implementation of a scalable, coupled-physics ASR model for simulating RC structures and assesses the ability of that model to predict ASR-induced expansion in recent laboratory tests on RC block and beam specimens. These laboratory tests and the simulation approach were selected because of their applicability to RC structural-scale simulations. This validation study helps builds confidence the ablility of this approach to model ASR expansion in large, complex RC structures, which is a current high-priority need.

## 1 | INTRODUCTION

Alkali-silica reaction (ASR) is an important concrete degradation mechanism involving complex dissolution-precipitation reactions that take place in the presence of alkali ions, silica, and moisture. Alkali ions diffuse from the hardened cement paste into the porous aggregate and start the silica dissolution by breaking silanol and siloxane bonds in the reactive aggregates. Hydrophilic silica gel, the key reaction product, is formed and expands in the presence of moisture[1]. The presence of silica gel initially does not exert any significant pressure on the surrounding concrete microstructure as it diffuses into the empty pore spaces. However, once the empty pore space is filled up or clogged due to calcification[2], the swelling silica gel applies internal pressure to the concrete microstructure. This applied hydrostatic stress results in aggregate and cement paste cracking at the microscopic level and can cause a loss of strength and stiffness, cracking, excessive expansion, and misalignment of structural components at the macroscopic level. Once this process begins, the ASR-induced cracking further accelerates ASR progression by enhancing reactant diffusion in the hardened cement paste and aggregates. While ASR has a detrimental effect on the material properties in the local affected regions, the volumetric expansion resulting from ASR can lead to elevated tensile stresses in other regions of the structure. This can thus cause cracking and reduction of structural capacity throughout a structure even when ASR is confined to some regions of a structure.

Since water acts as a solvent for silica dissolution and as a medium for ion diffusion through porous structures, moisture governs both the rate and magnitude of volumetric swelling[3, 4]. Apart from moisture, Ulm et al.[3] observed that both dissolution and diffusion mechanisms are thermoactivated chemical reactions. Furthermore, the state of stress is an important factor that governs the direction of ASR expansion[5]. There is general consensus from experimental data that compressive stresses limit the expansion in the directions of application and redistribute expansive strains to the directions with lower compressive stress. Experimental results indicate that triaxial confinement can delay or impede the extend of the volumetric expansion, although evidence on the extent of this effect is less conclusive, with some studies[6, 7] indicating that triaxial confinement slightly reduces volumetric expansion, while other indicate a more significant reduction[8, 9].

Due to the multiscale nature of ASR and its dependence on moisture, temperature, stress, and concrete material properties, researchers have developed a variety of methodologies to model ASR progression and its effects on concrete structures. Iskhakov et al.[10] summarized various techniques of modeling ASR in concrete structures including thermo-chemo-plastic, thermo-chemo-damage, and thermo-hygro-chemo-damage models for the structural-scale ASR effects. Modeling techniques from[1, 3, 11–13] include alkali diffusion into the porous aggregates and cement paste, permeation and imbibition of silica gel, presence of aggregates with varying reactivity, decrease in alkali concentration with the ASR progress, and ASR-induced damage on microstructure and structural scale. Multon et al.[14] developed a physiochemical model to estimate the volume of silica gel that can apply internal pressure based on mass-balance equations. This model considers a representative elementary volume to model various-sized aggregates as spheres to study the diffusion of alkali ions. The model estimates the ASR product (i.e., silica gel) volume over time assuming that it fills the pore spaces in the cement paste and aggregates. They utilized mechanical relationships to obtain the damaged elastic modulus and expansion of the representative elementary volume. Esposito and Hendriksa[15] summarized the modeling approaches based on the starting scale, input and output parameters, and solution technique (e.g., mathematical, analytical, or computational). Some models[13, 16, 17] focus on the microstructural scale but are difficult to utilize at structural scale. Other models[13, 16, 18–21] estimate gel swelling but do not predict its effects on mechanical properties and damage in concrete. Of particular interest for the present study are models targeted at structural-scale application that consider the simultaneous impact of temperature, relative humidity, and stress state[1, 3, 22–27]. Recent work with similar objectives has also used concurrent multiscale simulation methods, inform engineering-scale response with mesoscale models[28].

The present study is motivated by the need to model ASR progression and its effects on the performance of reinforced concrete (RC) structures, with a particular focus on engineering-scale assessment of containment vessels in nuclear power plants (NPPs). In light-water reactor NPPs, which are currently in widespread use worldwide, the containment vessel is designed to serve as a secondary barrier to the release of radioactive contaminants to the environment during the unlikely event of a breach in the primary coolant system. There are a variety of designs for containment vessels, employing steel, RC, or prestressed concrete. Concrete containment vessels are exposed to the same types of environmental conditions as other civil RC structures and are thus also generally subject to the same types of degradation mechanisms. While some concrete NPP structures, such as the biological shield wall, are exposed to high levels of radiation, which can cause structural degradation, the radiation doses experienced by containment vessels are negligible. ASR-induced degradation is potentially important for concrete containment vessels and has been observed in multiple operating NPPs. ASR, driven by the intrusion of moisture into subgrade structures, was observed at the Seabrook NPP in 2009[29]. ASR-induced expansion was reported in 1979 in the turbine generator foundation in Unit #1 of the Ikata NPP[30]. The expansion was caused by silicate minerals in andesite, which was present in the coarse aggregate. The expansion altered the distance between the generator's rotor axis and the bearing, which was mitigated by adjusting equipment. Containment vessels must withstand internal pressure loading in addition to the other loading they could be subjected to from external events such as seismic events[31, 32]. It is important to assess the effects of ASR or other degradation mechanisms on the ability of the containment vessel to withstand any of these loading conditions.

Because of its applicability to structural-scale simulations and ability to capture confinement effects, the Saouma and Perotti model[1], based on the earlier work of Ulm et al.[3] was employed here. Multiple published experimental studies on ASR are available for model validation. A number of these studies are particularly relevant to RC structures because they characterize the behavior of RC samples and structural members. The present study used experimental results from Wald et al.[33], Ballarini et al.[34] and Wald[35] for model validation because, in combination, they considered the effects of temperature, relative humidity, and rebar arrangement, which are the crucial factors governing the rate of ASR-induced expansion. More details about these studies are provided in Section 4. The scope of the present study is limited to addressing the progression of ASR and its mechanical effects including ASR-induced expansion, creep and damage, and structural deformation. While this is an important step toward addressing the effects of ASR on structural capacity and ductility, that is outside the scope of the present study and is an important topic of follow-on work.

The set of experimental results chosen for validation here is by no means exhaustive, and other recent experiments are also highly relevant for this purpose and are summarized below. Multon et al.[36] conducted an experimental study on RC beams with 500 mm depth, 250 mm width and 2,800 mm length, with varying levels of longitudinal reinforcement and a moisture gradient through the beam depths. They also considered the effect of increasing the alkali content in the concrete mix to accelerate the ASR expansion in the beam. They observed anisotropic swelling, the possibility of significant ASR expansion (0.1%), in the absence of an external water source, and the dominant influence of water on ASR expansion. Karthik et al.[37] studied the effect of severe ASR expansion on the load-carrying capacity of a C-beam specimen. The specimen has a rebar arrangement to achieve a state of stresses similar to that in a bridge pier. The concrete mix was prepared with a total alkali content of 5.9 $\frac{kg}{m^3}$ (with 1.9 $\frac{kg}{m^3}$ from NaOH). Over 5 years, the beam experienced heavy ASR deterioration and was tested mechanically. The load-carrying capacity was not reduced; however, stiffer load-deformation behavior and lower ductility were observed in the heavily deteriorated sample compared to slightly and moderately deteriorated beams. Habibi et al.[38] studied the effects of ASR on concrete shear walls subjected to 50°C and at least 95% relative humidity in an environmental chamber. Concrete mix proportions and age were the only variables changed between the shear wall specimens. ASR had a relatively minor effect on the load-carrying capacity of the shear walls, but under reverse cyclic and axial loading, the ASR degradation caused significant reductions in the ductility and energy dissipation capacity.

The experiments chosen for simulation here were selected because of their relevance to RC containment vessels. The cubes used rebars to provide varying levels of confinement, which is ideal for testing the approach used for modeling reinforcement. Both sets of beam experiments employed minimal or no transverse reinforcement, which is representative of the conditions in RC containment vessels. While it would certainly be worthwhile to extend the present validation study to include additional cases such as tests on prestressed concrete or shear walls, by necessity any validation effort must focus the available resources on a limited set of cases relevant to the target application.

The present validation effort focuses on predictions of the ASR-induced elongation measured in multiple directions, compared against experimental measurements. Because the specimens considered had a variety of reinforcement levels and arrangements, they are particularly useful for assessing the ability of the models to account for the effects of confining stresses, and in particular, the effects of anisotropic confinement. It is important to emphasize that there are other aspects of the model, such as the ASR effects on structural capacity and ductility, that are not assessed here, and should be addressed in future studies.

This paper first summarizes the governing equations and material models for temperature and moisture transport in concrete, ASR progression, behavior of rebars, and interactions between reinforcement and concrete in Section 2. Structural-scale simulations of ASR progression require solving large-scale, coupled-physics models. The computational framework used here is described in Section 3. Next, the validation study is described in Section 4, which includes descriptions of the experiments, computational models, and comparisons between experimental and simulation results. Finally, findings from this study are summarized in Section 5.

## 2 | GOVERNING EQUATIONS AND MATERIAL MODELS

The ASR progression and its effects on RC structure behavior are affected by the temperature and moisture distribution in the concrete and the mechanical deformation of and interactions between the concrete and rebar. A comprehensive simulation capability requires models for these phenomena and the interactions between them. The governing equations and material models for these phenomena are described here. As the focus of the present effort is on validation and application, the models for these various phenomena are all taken from other work, as noted in their respective descriptions. The primary novelty here is not in the models themselves, but in their implementation in a unified, open-source, parallel, multiphysics solution framework that is capable of practical, structure-scale simulations.

### 2.1 | Heat and moisture transfer

The standard heat equation governs heat transfer in concrete:

$$\rho C \frac{\partial T}{\partial t} = \nabla \cdot (k \nabla T) + Q \tag{1}$$

where $\rho$ is the density of concrete [kg/m$^3$], $C$ is the specific heat of concrete [J/kg °C], $T$ is the temperature [°C], $\boldsymbol{k}$ is the thermal conductivity of concrete [W/m °C], $Q$ is the rate of heat per unit volume generated within the body [W/m$^3$], and $t$ is time [$s$]. Thermal conductivity and capacity are dependent on the temperature as described in[39], which defines models that are applicable for both normal- and high-strength concrete.

The Xi[40] moisture model was used for moisture transfer in concrete. The governing equation for moisture transport is:

$$\frac{\partial W}{\partial H}\frac{\partial H}{\partial t} = \nabla \cdot \left(D_h \nabla H\right) \tag{2}$$

where $W$ is the total water content [g/g], $D_h$ is the moisture diffusivity [kg/ m$^2$ s], and $H$ is the pore relative humidity ($H = P_v/P_{vs}$), where $P_v$ is the vapor pressure and $P_{vs}$ is the saturate vapor pressure $\left(P_{\mathrm{atm}} \exp\left(4871.3\frac{T-100}{373.15T}\right)\right)$[41], where $T$ is the temperature in K and $P_{\mathrm{atm}}$ is the standard atmospheric pressure (101.325 Pa). The moisture transport model depends on the water-cement ratio, cement and aggregate type, aggregate pore type, cement and aggregate mass, aggregate volume fraction, and curing duration of the concrete. The estimation of the moisture diffusivity and moisture is described in[40]. In the current study, the mass matrix of the time derivative term of Equation (2) uses mass lumping to avoid spurious oscillations in the moisture profile caused in part by low moisture diffusivity.

## 2.2 | ASR swelling

As previously noted, the Saouma and Perotti model[1] was used for estimating ASR-induced swelling and damage in concrete structures. This model is based on the models of Larive[6] and Ulm et al.[3] for ASR kinetics, accounting for the temperature and relative humidity in the concrete microstructure, concrete strength in uniaxial tension, and compression, and builds onto that model by codifying a procedure to account for the effects of the local state of stress. This model is described in the next section.

### 2.2.1 | ASR kinetics

Under stress-free conditions, the extent of the ASR, $\xi$, can be expressed in terms of the volumetric strain, $\varepsilon$, as:

$$\xi(t) = \frac{\varepsilon(t)}{\varepsilon(\infty)} \tag{3}$$

where $\varepsilon(\infty)$ is the asymptotic volumetric strain when the ASR is complete. The ASR is assumed to follow $1^{st}$-order kinetics. Thus, the rate of ASR is expressed as:

$$\frac{d\varepsilon}{dt} = \frac{\varepsilon(\infty) - \varepsilon(t)}{t_c(T,\xi)} \tag{4}$$

where $t_c(T,\xi)$ is a characteristic time of reaction at a given temperature and is expressed as:

$$t_c(T,\xi) = \tau_C(T)\,\frac{1 + \exp\left(-\frac{\tau_L\left(T,I_\sigma,f_c'\right)}{\tau_C(T)}\right)}{\xi + \exp\left(-\frac{\tau_L\left(T,I_\sigma,f_c'\right)}{\tau_C(T)}\right)} \tag{5}$$

where $\tau_L\left(T, I_\sigma, f_c'\right)$ and $\tau_C(T)$ are the temperature-dependent characteristic time and latency time, respectively. Using Equations (4) and (5), the ASR extent can be rewritten as:

$$\xi(t) = \frac{1 - e^{\left(\frac{-t}{\tau_c}\right)}}{1 + e^{\left(\frac{-t}{\tau_c} + \frac{\tau_L}{\tau_c}\right)}} \tag{6}$$

The time constants for an arbitrary temperature can be computed from values at a reference temperature, $T_0$, (typically a temperature at which experimental data is gathered) by:

$$\tau_C(T) = \tau_C\left(T_0\right)\exp\left(U_C\left(\frac{1}{T} - \frac{1}{T_0}\right)\right) \tag{7}$$

$$\tau_L\left(T, I_\sigma, f_c'\right) = \tau_L\left(T_0\right) f\left(I_\sigma, f_c'\right)\exp\left(U_L\left(\frac{1}{T} - \frac{1}{T_0}\right)\right) \tag{8}$$

where $f\left(I_\sigma, f_c{}'\right)$ accounts for the effect of compressive stresses on impeding ASR and is defined as:

$$f\left(I_\sigma, f_c{}'\right) = \begin{cases} 1 & if \;\; I_\sigma > 0 \\ 1 + \alpha\frac{I_\sigma}{3f_c{}'} & if \;\; I_\sigma \le 0 \end{cases} \tag{9}$$

where $\sigma$ is the applied stress, $f_c^{\prime}$ is the uniaxial compressive strength of the concrete, $U_c$ and $U_L$ are the activation energy constants for characteristic time and latency, respectively, $I_\sigma$ is the first invariant of the stress tensor, and $\alpha$ is a stress dependency factor to couple chemical expansion with the mechanical phase. $\alpha$ is assumed to be equal to $\frac{4}{3}$ based on Multon's experimental results[42]. The latency time accounts for the absorption of silica gel in concrete pores. The latency period is proportional to the concrete porosity, as silica gel will take longer to fill highly porous concrete before ASR swelling can apply internal pressure to the aggregate and cement paste.

### 2.2.2 | ASR swelling mechanics

The expression for free volumetric expansion in concrete due to ASR, given in Equations (3) and (4), is updated to account for the effects of stress and relative humidity. The incremental volumetric expansion taking these effects into account, $\Delta\varepsilon_{\text{vol}}^{\text{ASR}}$ is expressed as:

$$\Delta\varepsilon_{\text{vol}}^{\text{ASR}}(t) = \Gamma_t\left(f_t^{\prime},\sigma_I\right)\Gamma_c\left(\bar{\sigma},f_c^{\prime}\right)g(H)\,\dot{\xi}(t,T)\,\varepsilon(\infty)\,|_{T=T_0} \tag{10}$$

where $f_t^{\prime}$ is the tensile strength of the concrete, $\sigma_I$ is the maximum principal stress (positive under tensile stress), $\bar{\sigma}$ (defined as $\frac{\sigma_I+\sigma_{II}+\sigma_{III}}{3f_c^{\prime}}$) is the ratio between the hydrostatic stress and compressive strength of concrete, and $\varepsilon(\infty)_{|T=T_0}$ is $\varepsilon(\infty)$ at the reference temperature. Here, $\Gamma_t$ accounts for the reduction in ASR swelling due to tensile cracking, which creates voids that can accommodate expanding silica gel. Similarly, $\Gamma_c$ represents a reduction in ASR swelling due to the diffusion of silica gel in the microcracks formed by compressive load[42]. $g(H)$ accounts for the dependency of gel expansion on the water in concrete. $\Gamma_t$, $\Gamma_c$, and $g(H)$ in (10) are computed as:

$$\Gamma_t = \begin{cases} 1 & if\ \left(\sigma_I \le \gamma_t f_t^{\prime}\right) \\ \Gamma_r + \left(1-\Gamma_r\right)\frac{\gamma_t f_t^{\prime}}{\sigma_I} & if\ \left(\gamma_t f_t^{\prime} \le \sigma_I\right) \end{cases} \tag{11}$$

$$\Gamma_c = \begin{cases} 1 & if\ \bar{\sigma} \le 0 \text{ tension} \\ 1 - \frac{e^{\beta}\bar{\sigma}}{1+\left(e^{\beta}-1\right)\bar{\sigma}} & if\ \bar{\sigma} > 0 \text{ compression} \end{cases} \tag{12}$$

$$g(H) = H^m \tag{13}$$

where $\gamma_t$ is the fraction of the yield strength beyond which the silica gel can accommodate space created due to cracking, $\Gamma_r$ is the residual ASR retention factor in tensile loading, and $\beta$ and $m$ are empirical constants.

As observed experimentally[6,7], ASR swelling occurs preferentially in directions where stress is less compressive. The procedure of[1], which was employed here, accounts for those observations in distributing the volumetric strain in the three principal stress directions, corresponding to principal stresses $\sigma_l$, $\sigma_m$, and $\sigma_n$. Weights, $W_k$, for the fraction of the total volumetric strain increment applied in each principal direction, $k$, are defined such that the total of the weights in the three directions is one.

The weights are computed based on observed behavior when the concrete is in uniaxial, biaxial or triaxial loading and are defined for a given direction $k$ for three cases for the stress in each direction: 1) the stress is tensile or zero, 2) the stress is equal to a compressive stress beyond which no further gel expansion can occur, $\sigma_u$ (indicated to be -10 MPa by the experimental studies of[6]), or 3) the stress is equal to the compressive strength, $f_c^{\prime}$. The weight factors for a given principal stress, $\sigma_k$, based on the other two principal stresses, $\sigma_l$ and $\sigma_m$, for these discrete stress combinations are given in Table 1. The stresses typically fall between these points, so trilinear interpolation is used to compute a weight factor for each direction between the points in the principal stress space in Table 1 that bound the three principal stress components. Once these weights are computed, the increment in volumetric strain in each principal stress direction $i$ can be calculated as:

$$\Delta\varepsilon_{vol|i}^{ASR} = W_i\Delta\varepsilon_{\text{vol}}^{\text{ASR}}\forall i = \{1,2,3\} \tag{14}$$

These strains are then applied in their corresponding principal directions.

As discussed in Section 1, ASR causes degradation in both the tensile strength and elastic stiffness of concrete. The decrease in elastic stiffness depends on both temperature and the ASR extent, according to:

$$\begin{aligned} \mathbb{C} &= \left(1-d_{\text{ASR}}\right)\mathbb{C}_0 \\ d_{\text{ASR}}(t,T) &= \left(1-\beta_C\right)\xi(t,T) \end{aligned} \tag{15}$$

where $\mathbb{C}$ and $\mathbb{C}_0$ are the damaged and undamaged elastic stiffness of concrete, respectively, $d_{\text{ASR}}$ is the extent of the ASR damage, and $\beta_C$ is the fractional residual elastic stiffness and tensile strength after the ASR has completed. In the model of[1], the concrete's tensile strength is directly reduced by ASR-induced damage. The procedure used here differs somewhat from that and is described in Section 2.4.

**Table 1** Weights for the distribution of ASR strain in direction $k$ based on principal stress values $\sigma_l$, $\sigma_m$, and $\sigma_k$ for key discrete stress values (adapted from[1]). Note that tensile stresses are positive by convention.

| | | Weight for Direction $k$ | | |
|---|---|---|---|---|
| $\sigma_l$ | $\sigma_m$ | $\sigma_k \geq 0$ | $\sigma_k = \sigma_u$ | $\sigma_k = f'_c$ |
| $\geq 0$ | $\geq 0$ | 1/3 | 0 | 0 |
| $\sigma_u$ | $\geq 0$ | 1/2 | 0 | 0 |
| $\sigma_u$ | $\sigma_u$ | 1 | 1/3 | 0 |
| $\geq 0$ | $\sigma_u$ | 1/2 | 0 | 0 |
| $f_c$ | $\geq 0$ | 1/2 | 0 | 0 |
| $f_c$ | $\sigma_u$ | 1 | 1/2 | 0 |
| $f_c$ | $f_c$ | 1 | 1 | 1/3 |
| $\sigma_u$ | $f_c$ | 1 | 1/2 | 0 |
| $\geq 0$ | $f_c$ | 1/2 | 0 | 0 |

## 2.3 | Concrete creep

Stresses in concrete due to ASR expansion can be significant, so it is important to account for creep in simulations of the long-term effects of ASR on RC structures. The logarithmic viscoelastic creep model described by Giorla[43] is used here to account for concrete creep. Deformation is represented by a generalized Kelvin model consisting of three modules in series: a spring, a Kelvin-Voigt unit with a spring and dashpot, and a final dashpot. The total strain, $\varepsilon$, is decomposed by these modules into the elastic strain, $\varepsilon_e$, the partly recoverable short-term creep strain, $\varepsilon_r$, and the irrecoverable long-term creep strain, $\varepsilon_v$, respectively. The viscoelastic strain represented by the Kelvin-Voigt module is partly recoverable upon unloading. The irrecoverable creep strain is linear with the logarithm of time and cannot be recovered upon unloading. The strain decomposition is expressed as:

$$\boldsymbol{\varepsilon} = \boldsymbol{\varepsilon_e} + \boldsymbol{\varepsilon_r} + \boldsymbol{\varepsilon_v} \tag{16}$$

The same stress, $\boldsymbol{\sigma}$, is applied to each module and is related to the strains in the individual modules as:

$$\boldsymbol{\sigma} = \mathbb{C}_e : \boldsymbol{\varepsilon_e} \tag{17}$$

$$\boldsymbol{\sigma} = \mathbb{C}_r : \left(\boldsymbol{\varepsilon_r} + \eta_r \dot{\boldsymbol{\varepsilon}}_r\right) \tag{18}$$

$$\boldsymbol{\sigma} = \left(1 + \frac{t}{\tau_v}\right) \eta_v \mathbb{C}_e : \dot{\boldsymbol{\varepsilon}}_v \tag{19}$$

where $\mathbb{C}_e$ is the elasticity tensor, $\mathbb{C}_r$ is the recoverable elasticity tensor of the spring in the Kelvin-Voigt unit, $\eta_r$ is the recoverable viscosity, $\eta_v$ is the long-term viscosity, and $\tau_v$ is the long-term characteristic time. The elasticity tensors are computed based on user-supplied Poisson's ratio, Young's modulus, and recoverable Young's modulus.

This model considers the effect of temperature by defining temperature-dependent values of the long-term viscosity, $\eta_v(T)$, and recoverable viscosity, $\eta_r(T)$:

$$\eta_v(T) = e^{\left(T_a\left(\frac{1}{T} - \frac{1}{T_{\text{ref}}}\right)\right)} \eta_v\left(T_{\text{ref}}\right) \tag{20}$$

$$\eta_r(T) = e^{\left(T_a\left(\frac{1}{T} - \frac{1}{T_{\text{ref}}}\right)\right)} \eta_r\left(T_{\text{ref}}\right) \tag{21}$$

where $T_a$ is an activation temperature and $T_{\text{ref}}$ is the reference temperature at which reference viscosities $\eta_v\left(T_{\text{ref}}\right)$ and $\eta_v\left(T_{\text{ref}}\right)$ are defined.

Similarly, the effects of relative humidity are accounted for by defining the humidity-dependent recoverable elasticity tensor, $\mathbb{C}_r(H)$, and long-term viscosity $\eta_v(H)$:

$$\mathbb{C}_r(H) = \frac{1}{H}\mathbb{C}_r\left(H_{\text{ref}}\right) \tag{22}$$

$$\eta_v(H) = \frac{1}{H}\eta_v\left(H_{\text{ref}}\right) \tag{23}$$

where $H_{\text{ref}}$ is a reference humidity at which the reference values of $\mathbb{C}_r\left(H_{\text{ref}}\right)$ and $\eta_v\left(H_{\text{ref}}\right)$ are defined.

## 2.4 | Concrete damage

Damage induced by ASR can be due to local damage incurred by the ASR and mechanical damage induced by stresses resulting from by the ASR volumetric expansion, as well as other loadings to the structure. The model for local ASR-induced damage was described in Section 2.2.2. Because that local ASR damage is based on a scalar damage parameter, using a similar approach for other strain-induced (i.e., mechanical) damage makes combining those effects straightforward. The Mazars damage model[44, 45] is an isotropic damage model that can model the stiffness degradation and softening behavior of the concrete and is employed here. In the Mazars model, a scalar mechanical damage variable $d_m$ is expressed as a combination of tension and compression damage modes:

$$d_m = \alpha_t d_t + \alpha_c d_c \tag{24}$$

where $\alpha_t$ and $\alpha_c$ are coefficients that depend on the strain orientation and $d_t$ and $d_c$ are damage variables for tension and compression, respectively. These $\alpha$ coefficients account for the contributions of tensile and compressive loading and are computed as:

$$\alpha_t = \sum_{i=1}^{3} \left( \frac{\langle \epsilon_i^t \rangle \langle \epsilon_i \rangle}{\tilde{\epsilon}^2} \right)^{\beta} \tag{25}$$

$$\alpha_c = \sum_{i=1}^{3} \left( \frac{\langle \epsilon_i^c \rangle \langle \epsilon_i \rangle}{\tilde{\epsilon}^2} \right)^{\beta} \tag{26}$$

where the exponent $\beta$ is a user-defined parameter that can be adjusted to fit the material response to the experimental data for shear response, $\langle \epsilon_i^t \rangle$ and $\langle \epsilon_i^c \rangle$ are the principal components of the strain tensors resulting from the tensile and compressive components of the stress tensor, and $\langle \epsilon_i \rangle$ contains the principal components of the strain tensor. The tensile and compressive damage variables are computed as:

$$d_t = 1 - \frac{\kappa_0 \left(1 - A_t\right)}{\kappa} - \frac{A_t}{\exp\left[B_t \left(\kappa - \kappa_0\right)\right]} \tag{27}$$

$$d_c = 1 - \frac{\kappa_0 \left(1 - A_c\right)}{\kappa} - \frac{A_c}{\exp\left[B_c \left(\kappa - \kappa_0\right)\right]} \tag{28}$$

where $A_t$, $A_c$, $B_t$, and $B_c$ are material parameters that affect the shape of the nonlinear response and $\kappa$ defines the damage evolution threshold, which initially has the value $\kappa_0 = \frac{f_t}{E_0}$, where $f_t$ is the tensile strength and $E_0$ is the initial Young's modulus of the material. As the damage evolves, $\kappa$ is determined for each load step as:

$$\kappa = \max\left(\tilde{\epsilon}, \kappa_0\right) \tag{29}$$

where $\tilde{\epsilon}$ is an equivalent strain quantity calculated from the positive eigenvalues of the strain tensor as:

$$\tilde{\epsilon} = \sqrt{\sum_{i=1}^{3} (\langle \epsilon_i \rangle_+)^2} \tag{30}$$

where $\epsilon_i$ are the components of principal strain and $\langle . \rangle_+$ is the Macaulay bracket, defined as:

$$\langle \epsilon_i \rangle_+ = \begin{cases} \epsilon_i & \epsilon_i > 0 \\ 0 & \epsilon_i <= 0 \end{cases} \tag{31}$$

The coefficients $A_t$, $A_c$, $B_t$, and $B_c$ are calibrated to match the peak strength and softening behavior of the concrete under uniaxial tension and compression.

The combined effects of ASR-induced damage and mechanical damage are accounted for by computing the damage for the mechanical damage and ASR models at each quadrature point and then computing a combined damage index $d_{\mathrm{comb}}$ as:

$$d_{\mathrm{comb}} = 1 - \left(1 - d_m\right)\left(1 - d_{\mathrm{ASR}}\right) \tag{32}$$

This combined damage index is used to degrade the material stiffness and stress. It should be noted that in this approach for combining ASR and mechanical damage, ASR-induced damage degrades both the tensile and compressive strength of the concrete, while an approach in which ASR only decreases tensile strength would be preferred[1, 26, 28]. The Mazars damage model does not readily allow for ASR-induced damage to only affect the tensile behavior, so a different mechanical damage model would be required to incorporate this behavior. Additionally, to avoid numerical issues, the damage can be limited to a user-specified value below 1.0, which gives a small amount of residual strength.

## 2.5 | Steel reinforcement

Steel reinforcement in concrete can be modeled in a number of ways, including using rebar properties distributed through the concrete, discrete bars, or rebar layers embedded within the concrete matrix. Steel reinforcement is modeled here using one dimensional (1D) line elements that mechanically behave as trusses (i.e., axial resistance but no bending resistance) and conduct heat along their axis. These are embedded within a two or three dimensional (2D or 3D) finite element model of the concrete matrix. To facilitate model setup, constraints are imposed on the rebar nodes to enforce compatibility between their displacement and temperature and that of the matrix material at the rebar node locations, which can be anywhere within the concrete matrix elements. The use of these constraints allows the rebar and concrete to be meshed independently, so they do not need to share nodes. It is important to note that the way displacement compatibility between rebar and matrix is enforced here assumes a perfect bond. Incorporating a bond-slip model would permit realistic representation of confinement, particularly near the ends of bars or in regions with significant damage, where slip could be significant for many of the cases considered here. This is an area for future development.

The mechanical behavior of the rebar is described by a model that assumes the axial response is linearly elastic, followed by linear strain hardening above the yield stress. The model also includes axial heat conduction along rebar using constant thermal conductivity and specific heat. Thermal expansion is also modeled in the rebar, using a constant coefficient of thermal expansion. This study did not assume any strain hardening (i.e., perfect plasticity) because yielding in the rebar modeled here is followed by a plateau region in which the bar has a nearly perfectly plastic response before strain hardening. The strain in the rebar only slightly exceeded where strain hardening begins in one of the simulations performed here. Higher strains would warrant using a more complete hardening curve.

## 3 | IMPLEMENTATION OF MULTIPHYSICS MODELS IN THE BLACKBEAR CODE

To maximize the ability to account for interactions between the physics models for heat and moisture transport and mechanical deformation in the presence of ASR described in Section 2, it is important to implement those models in a software framework designed to handle multiphysics coupling. In addition, to perform detailed simulations of large-scale structures, it is essential to take advantage of modern high-performance computing hardware, through parallel solution algorithms. To meet these needs, these models were implemented in BlackBear[46], which is a code based on the open-source Multiphysics Object-Oriented Simulation Environment (MOOSE) framework[47].

MOOSE is designed specifically to meet the needs of large-scale, multiphysics simulations, providing the ability to solve systems of coupled-physics equations either in a single nonlinear solution or using staggered solution schemes, and relies on both the foundational capabilities to solve finite element models provided by the libMesh[48] library and the scalable solvers provided through the PETSc[49] library. MOOSE has a modular structure for defining the various aspects of a physics solution, with C++ base classes that define the interfaces developers can specialize to create code objects for specific purposes. MOOSE manages the execution of these objects, so application codes such as BlackBear can readily expand on the capabilities in MOOSE by adding modules, with no need to modify code execution logic.

BlackBear is an open-source subset of the capabilities of the access-controlled Grizzly code[46], which addresses aging issues in NPP systems, components, and structures. Grizzly contains capabilities specific to NPPs, such as models for radiation-induced volumetric expansion[50] in concrete (which build on multiple aspects of the ASR models described here), but the capabilities demonstrated in this paper for modeling thermal and moisture transport in concrete, ASR progression, and ASR effects on the mechanical behavior, rebar behavior, and constraints between rebar and concrete are open source, implemented in BlackBear or MOOSE, which are accessible through code repositories hosted by GitHub[51, 52]. Most of the ASR models were originally developed in in Grizzly[53, 54], but were subsequently made open-source and moved to BlackBear.

## 4 | VALIDATION AGAINST ACCELERATED LABORATORY TESTS

The modeling framework to simulate the ASR-induced degradation in RC is validated here using results from the experimental studies on material- and structural-scale specimens. The validation cases include RC blocks with varying steel rebar confinement, RC beams subjected to time-varying temperature and moisture conditions, and different rebar arrangements.

### 4.1 | Free expansion of concrete blocks

Wald et al.[33] performed a series of experiments to understand how reinforcement affects ASR expansion behavior in concrete. Their study monitored the free expansion, in three axial directions of four plain concrete cubes and 33 RC cubes with varying reinforcement configurations, all having an edge length of 480 mm, under controlled environmental temperature and humidity conditions. These experiments are well-suited to assess and validate the ASR models, in particular the model aspect that accounts for the effect of confinement, and their results are compared to simulation results here.

Some of these experiments are modeled here, including an unreinforced block (Specimen A1-000b, in the nomenclature of[33], which is used throughout this section), and several blocks with varying reinforcement configurations. Experimental data is available for an additional unreinforced specimen (A1-000a) and is in general agreement with the specimen used here, except for a somewhat greater expansion in one direction. Because of the greater consistency between the expansion observed in the three directions in A1-000b, it is used here for calibration. Figure 1 shows the finite element models of these blocks with rebar modeled as 1D trusses. It shows the configuration of the reinforcement bars oriented in the $x$-, $y$-, and $z$-directions distributed in either two or three layers, depending on the experiment. The model of the unreinforced block is not shown here but is identical to the models shown, except for the absence of rebar. The details of the various rebar configurations used in the experiments, using data on specific rebar sizes from[55], are provided in Table 2. The naming convention of[33] for the specimens is followed here.

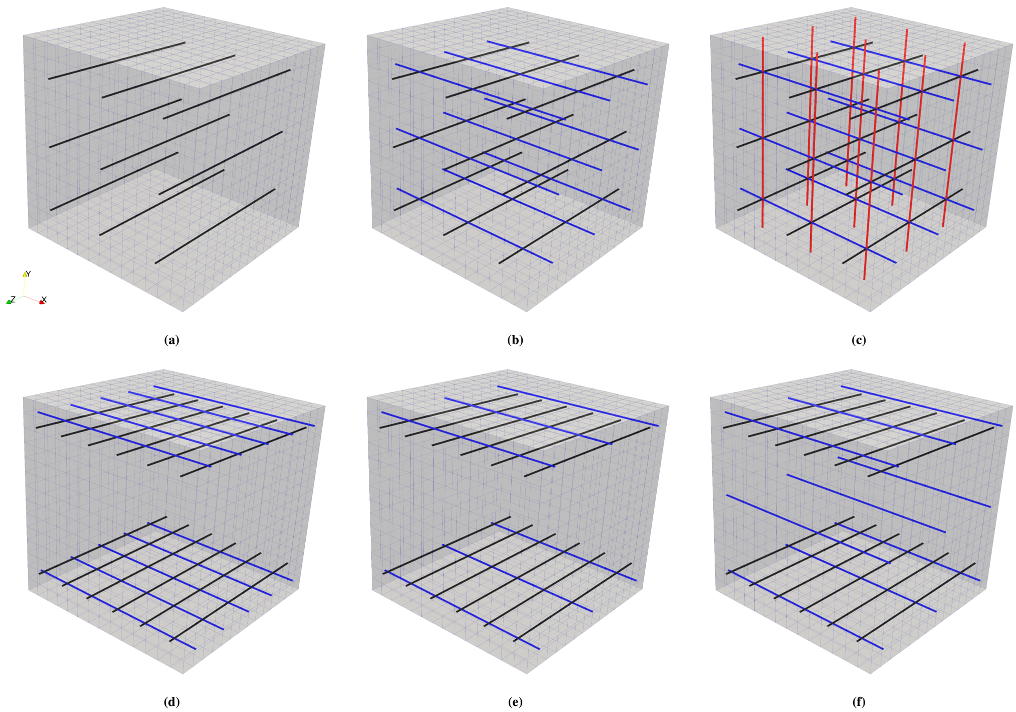


**Figure 1** Finite element model of concrete blocks with various reinforcement configurations: (a) Uniaxial, (b) Biaxial, (c) Triaxial, (d) Biaxial-L1, (e) Biaxial-L2, and (f) Biaxial-L3.

The multiphysics models of these blocks solve for temperature, relative humidity, and displacement fields using the models described in Section 2. The mechanical deformation of the blocks includes the effects of ASR expansion, thermal strain in the rebar and concrete, and creep in the concrete. To model free expansion, the blocks are unrestrained in all directions and the only mechanical boundary conditions applied are pinned nodes to prevent rigid body motion. For the thermal and humidity boundary conditions, experimental temperature and humidity histories[33], as shown in Figure 2, are applied on all outside concrete block boundaries. Because anchors were used at the ends of the rebars in these block experiments, the modeling assumption of perfect bond used here is appropriate. Table 3 summarizes the material properties used in the simulations. Most of these properties, including those related to transport, elasticity, creep and damage are chosen to be generally appropriate for concrete having the strength of that tested in the experiments. The main parameters that were calibrated were those pertaining to ASR expansion, in particular the latency and characteristic time and maximum ASR volumetric expansion. Those ASR-related parameters were calibrated to match the average axial expansion observed in the plain concrete block (A1-000b), and then applied to the other blocks in this series.

**Table 2** Configuration details of the concrete block specimens.

| Reinforcement Arrangement | Specimen Name | Reinforcement Bars/Area Percentage | | | Model Configuration |
|---|---|---|---|---|---|
| | | x-direction | y-direction | z-direction | |
| Unreinforced | A1-000b | - | - | - | Figure 1, no rebar |
| Uniaxial | A1-001a/b | - | - | 9#4 bars (0.5%) | Figure 1a |
| | A1-002 | - | - | 9#6 bars (1.1%) | |
| | A1-003 | - | - | 9#7 bars (1.5%) | |
| Biaxial (3 layer) | A1-101a/b | 9#4 bars (0.5%) | - | 9#4 bars (0.5%) | Figure 1b |
| | A1-102a | 9#4 bars (0.5%) | - | 9#6 bars (1.1%) | |
| | A3-102c | 9#4 bars (0.5%) | - | 9#6 bars (1.1%) | |
| | A1-103 | 9#4 bars (0.5%) | - | 9#7 bars (1.5%) | |
| | A1-202 | 9#6 bars (1.1%) | - | 9#6 bars (1.1%) | |
| | A1-303 | 9#7 bars (1.5%) | - | 9#7 bars (1.5%) | |
| Biaxial (2 layer) | A3-102-L1 | 10#4 bars (0.6%) | - | 12#5 bars (1.0%) | Figure 1d |
| | A3-202-L2 | 6#7 bars (1.0%) | - | 12#5 bars (1.0%) | Figure 1e |
| | A3-202-L3 | 9#6 bars (1.1%) | - | 12#5 bars (1.0%) | Figure 1f |
| Triaxial | A1-111a/b | 9#4 bars (0.5%) | 9#4 bars (0.5%) | 9#4 bars (0.5%) | Figure 1c |
| | A1-222 | 9#6 bars (1.1%) | 9#6 bars (1.1%) | 9#6 bars (1.1%) | |
| | A1-211 | 9#6 bars (1.1%) | 9#4 bars (0.5%) | 9#4 bars (0.5%) | |
| | A1-331 | 9#7 bars (1.5%) | 9#7 bars (1.5%) | 9#4 bars (0.5%) | |
| | A1-321a | 9#7 bars (1.5%) | 9#6 bars (1.1%) | 9#4 bars (0.5%) | |

Figure 2 compares the computed average temperature and relative humidity within the plain concrete block resulting from the applied boundary conditions. In the simulations, the average temperature response of the block closely follows the environmental temperature prescribed on the block boundaries because heat conduction occurs rapidly relative to the time scale of the experiment. In contrast, due to the low permeability of the concrete, moisture transport occurs over much longer time scales, so the average value of the relative humidity does not track the value at the boundary as closely as does the temperature. Experimental data is not available to validate the simulated interior temperature and relative humidity, but the simulated behavior appears reasonable.

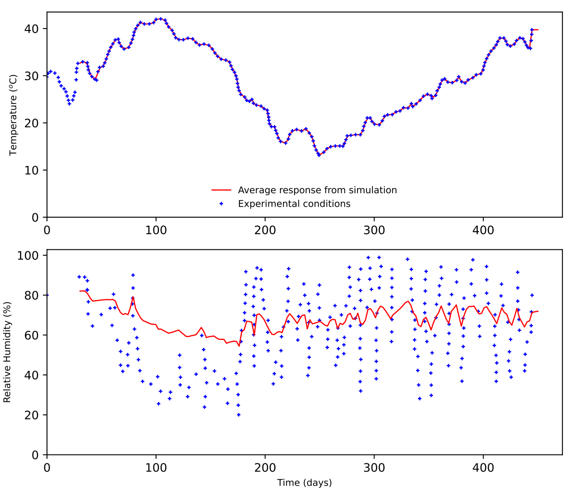


**Figure 2** Time history of temperature (top) and relative humidity (bottom) for concrete blocks, showing volume-averaged values from a plain concrete block (A1-001a) plotted against reported experimental environmental conditions[33], which were applied as boundary conditions to the model. Results for the A1-series RC blocks are not shown but are nearly identical to these.

The axial expansion reported from the experiments includes the effects of all sources of strain, including shrinkage, creep, ASR and thermal expansion. The displacement values were extracted from the simulation at the same six points that were considered

**Table 3** Concrete and rebar properties for simulating the Wald et al. blocks.

| | **Material Property** | **Value** |
|---|---|---|
| Initial Conditions | Initial relative humidity | 80% |
| | Initial and stress-free temperature | 30°C |
| Concrete Transport | Heat transport model | Eurocode-2004 |
| | Moisture transport model | Xi |
| | Aggregate pore type | Dense |
| | Cement type | U.S. Type I |
| | Aggregate volume fraction | 0.7 |
| | Aggregate mass | 1877 kg/m$^3$ |
| | Cement mass | 354.0 kg/m$^3$ |
| | Reference density of concrete ($\rho$) | 2231.0 kg/m$^3$ |
| | Reference specific heat of concrete ($C$) | 1100.0 J/(Kg K) |
| | Water-cement ratio | 0.5 |
| ASR Expansion and Damage | Concrete cure time | 28 days |
| | Reference temperature for ASR expansion ($T_0$) | 35°C |
| | Max ASR volumetric expansion ($\varepsilon(\infty)$) | 0.025 |
| | Characteristic time ($\tau_C$) | 35 days |
| | Latency time ($\tau_L$) | 18 days |
| | Characteristic time activation energy ($U_C$) | 5400.0 K |
| | Latency time activation energy ($U_L$) | 9400.0 K |
| | Stress latency factor ($\alpha$) | 1 |
| | Compressive stress exponent ($\beta$) | 1 |
| | Expansion stress limit ($\sigma_u$) | 8.0 MPa |
| | Tensile retention factor ($\Gamma_r$) | 1 |
| | Tensile absorption factor ($\Gamma_t$) | 1 |
| | Relative humidity exponent for ASR volumetric strain ($m$) | 1 |
| | Compressive strength ($f_c'$) | 31 MPa |
| | Tensile strength ($f_t'$) | 3.1 MPa |
| | Fractional residual elastic stiffness ($\beta_C$) | 0.7 |
| Thermal Expansion | Concrete thermal expansion coefficient | 8.0 $\times 10^{-6}$ 1/K |
| | Rebar thermal expansion coefficient | 11.3 $\times 10^{-6}$ 1/K |
| | Rebar thermal conductivity | 45 W/(m K) |
| Concrete Mechanical | Viscoelastic model | Logarithmic creep |
| | Concrete Young's modulus | 37.3 GPa |
| | Concrete Poisson's ratio | 0.22 |
| | Recoverable Young's modulus | 19.9e9 GPa |
| | Recoverable viscosity ($\eta_r$) | 2592000 s |
| | Long-term viscosity ($\eta_v$) | 138240000 s |
| | Long-term characteristic time ($\tau_v$) | 138240000 s |
| | Reference temperature for creep ($T_{\text{ref}}$) | 23°C |
| | Reference relative humidity for creep ($H_{\text{ref}}$) | 1 |
| | $\beta$ exponent for Mazars damage | 1 |
| | $A_t$ coefficient for Mazars damage | 0.9 |
| | $A_c$ coefficient for Mazars damage | 1 |
| | $B_t$ coefficient for Mazars damage | 16000 |
| | $B_c$ coefficient for Mazars damage | 1600 |
| | Maximum scalar damage | 0.95 |
| Rebar Mechanical | Rebar Young's modulus | 200 GPa |
| | Rebar yield stress | 415 MPa |

during the experiments[33], on each of the surfaces. The average expansion reported here is the average of the measurements from these six points, which similar to the experimental data include all sources of strain, although it is important to note that shrinkage is not include in the model. The starting times for all presented results for the blocks are the casting times, which are assumed to be 28 days before exposure to the environment conditions. Figure 3 shows the experimental and simulation results, which indicate that, with calibration, the model can replicate the experimentally observed behavior reasonably well.

The same set of parameters obtained from the model calibration for the unreinforced block were then used to predict the expansion of the RC blocks. Time histories of the simulated average axial expansion in the three directions compared with experimental results of various concrete block specimens are shown in Figure 4. For the A1 specimens, the model predictions generally follow the experimental observations. The constraining effect of the rebar is clearly evident as a decreased expansion in the reinforced direction relative to the directions with no reinforcement. There is also a clear dependence in the response on

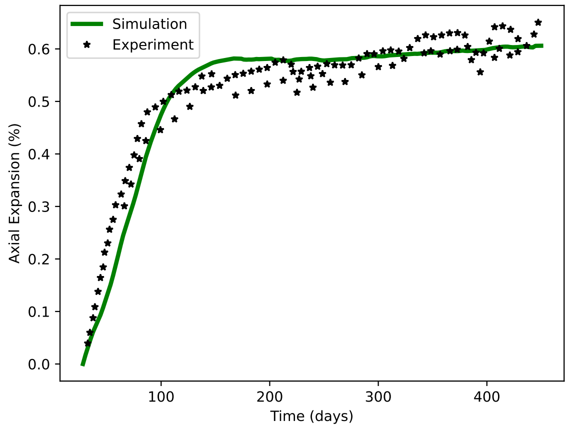


**Figure 3** Time history of the axial expansion of an unrestrained plain concrete block (A1-000b), comparing calibrated simulation results with experimental data.

the rebar fraction in a given direction, which was adjusted by varying the nominal diameter of the rebar as mentioned in Table 2. For example, there is a clear trend of decreasing expansion in the $z$-direction as the nominal reinforcement is increased from 0.5% to 1.5% over uniaxially reinforced specimens A1-001a, A1-002, and A1-003. Many cases (e.g., A1-001a and A1-101a) have identical reinforcement in two directions, so the simulated response is nearly identical in those two directions. In cases where there is different reinforcement in all three directions (e.g., A1-103 and A1-321), the simulations indicate significant differences in expansion in the three directions, with greater expansion predicted in the directions with less reinforcement. This behavior is also observed in the experimental results, with some minor deviations.

Note that there are multiple pairs of specimens (A1-001a and A1-001b, A1-101a and A1-101b, and A1-111a and A1-111b) that have identical experimental conditions and rebar arrangements, so a single simulation is compared with those two different experimental results. There is fairly significant variation between the experimental observations for all three pairs of experiments, which is likely indicative of the expected variation in other specimens.

The A3 specimens were cast and tested later during the same environmental exposure period that the A1 specimens were subjected to and use the same concrete mix as the A1 specimens. While one of the A3 specimens employs the same reinforcement arrangement as the A1 specimens (A3-102), the other three A3 specimens used different arrangements, indicated by the suffix. In all these cases, the effects of changing the rebar arrangement with the same nominal areas are small. The differences between A3-102c and A3-102-L1 are noticeable, but this can largely be attributed to differences in the nominal areas between the rebar arrangements. For all A3 specimens, the simulations overpredict the experimentally observed expansion, particularly in the directions confined by reinforcement. The ASR model parameters used in the A3 specimen simulations are the same as those for the A1 specimens because they were reported to be the same mix. There is, however, clearly a systematic difference between the behavior of the A1 and A3 specimens. While the ASR expansion parameters could be recalibrated specifically for the A3 specimens, there is no unreinforced A3 specimen available for calibration, and the value of that exercise is questionable because there are no available data on what might have differed between the A1 and A3 specimens.

## 4.2 | Reinforced concrete beams

While the study on RC blocks in Section 4.1 demonstrates that the effects of confinement on deformation with varying reinforcement are reasonably captured in the ASR model for simple specimens, it is important to also validate the model on more complex specimens with geometries closer to those of actual structural members. Two recent series of tests on RC beams provide useful data for such validation. This study considered three RC beams from the experiments at the University of Southern California (USC) reported in [34] and one beam from experiments at the University of Texas (UT), Austin [35]. These experiments are considered in the following sections.

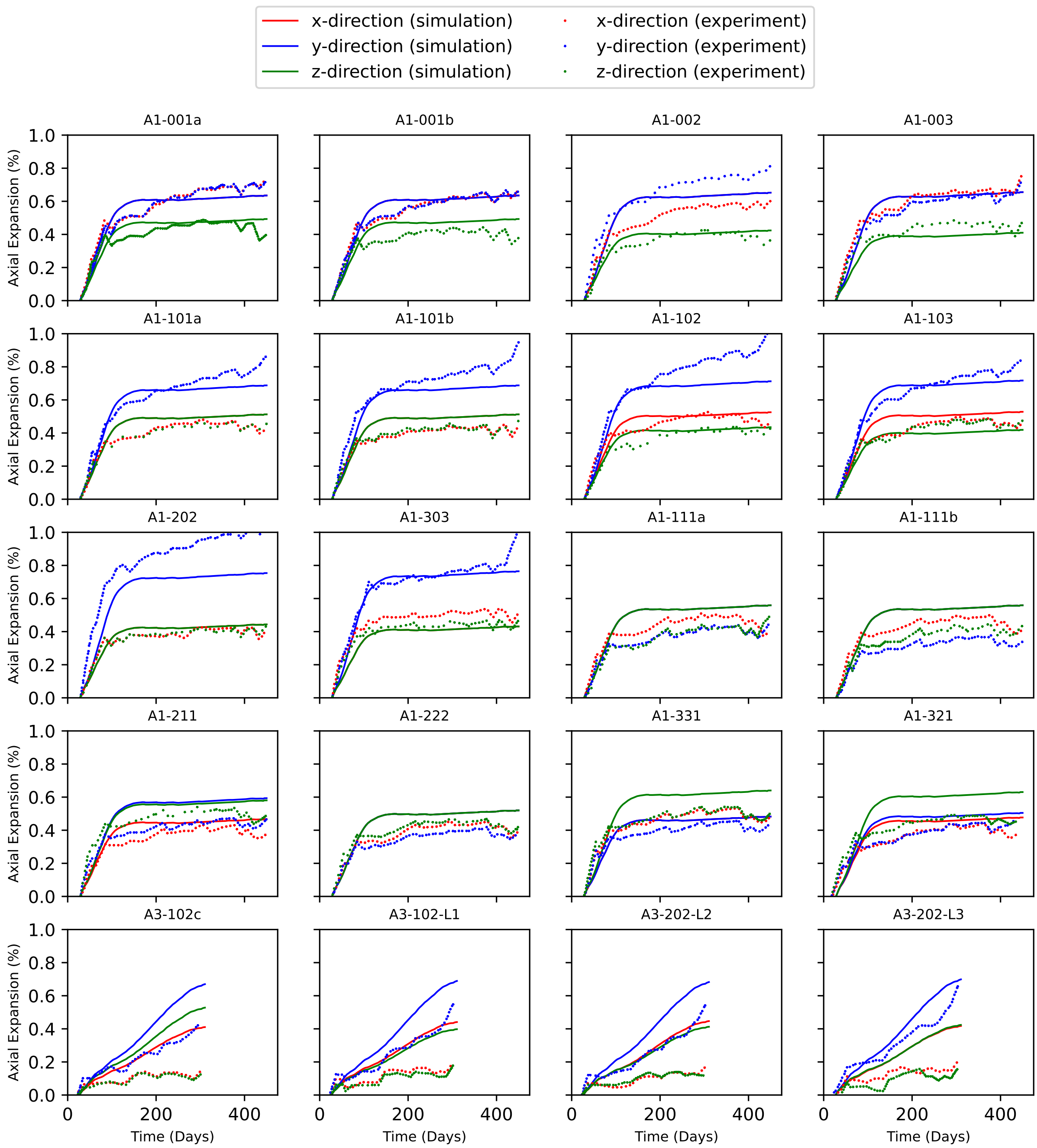


**Figure 4** Free expansion of various RC block specimens, with comparisons between the axial expansion predicted by simulations and the experimental observations.

#### 4.2.1 | University of Southern California beams

Multiple RC beams were tested under conditions that resulted in accelerated ASR at USC, as documented by Ballarini et al.[34] and Gencturk et al.[56]. A total of six beams, Beams 1–6, were tested. The beams had similar geometry and rebar arrangements, but the environmental conditions and mix proportions varied for each beam. All beams had a 610 mm depth, 305 mm width, and 6,401 mm length. Beams 1–3 were loaded to assess their structural capacity with ASR, while Beams 4–6 (the cases considered here) were only monitored for expansion. Beam 4 was subjected to the laboratory environment, while Beams 5 and 6 were subjected to the ambient environment in Los Angeles, CA. Beams 4 and 5 were constructed using the same mix proportions without any alkali content, while Beam 6 has a 1.25% NaOH solution by weight of cement to accelerate ASR. All beams were designed to have a shear span on each side to be exercised during mechanical testing. The axial reinforcement was uniform along the span, but there was more shear reinforcement in the middle of the span than on the shear spans on the sides of the beam, which resulted in lower confinement against ASR expansion than in the mid-span region.

The finite element model of the USC beams is shown in Figure 5, which highlights the heavy and light confinement region zones. The modeling parameters for the beam are indicated in Table 4 and as for the block tests, the ASR-related parameters were calibrated based on tests of prisms cast from the concrete mixes used for the beams. Because they had the same concrete mix proportions, the maximum ASR volumetric expansion parameter is considered the same for Beams 4 and 5. Since concrete mix proportions are different for Beam 6 as compared to Beams 4 and 5, the maximum ASR volumetric expansion for Beam 6 is increased by the same ratio as observed for prism specimens, which were tested for each concrete batch used to construct the beams.

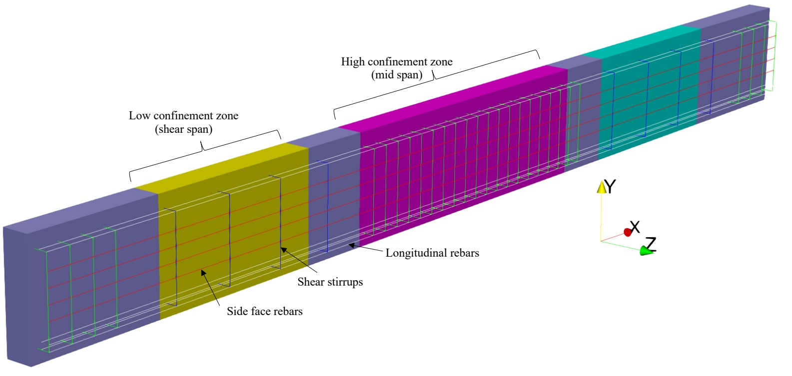


**Figure 5** Finite element model of the USC RC beams, showing the zones with varying confinement. The front half of the concrete is clipped by the $z$-plane to show the arrangement of rebar, modeled as truss elements.

**Table 4** Modeling parameters for RC beams that differ from or supplement those reported in Table 3.

| Parameter | USC Beam 4 | USC Beam 5 | USC Beam 6 | UT Beam |
|---|---|---|---|---|
| Cement type | U.S. Type II | U.S. Type II | U.S. Type II | U.S. Type II |
| Reference thermal conductivity of concrete | 3 W/(m K) | 3 W/(m K) | 3 W/(m K) | 3 W/(m K) |
| Concrete cure time | 14 days | 14 days | 14 days | 56 days |
| Aggregate mass | 2407.0 kg/m$^3$ | 2407.0 kg/m$^3$ | 2407.0 kg/m$^3$ | 1877.0 kg/m$^3$ |
| Water-cement ratio | 0.52 | 0.52 | 0.52 | 0.50 |
| Reference temperature for ASR expansion ($T_0$) | 23.0°C | 23.0°C | 23.0°C | 35.0°C |
| Max ASR volumetric expansion ($\varepsilon(\infty)$) | 0.03 | 0.03 | 0.06 | 0.027 |
| Characteristic time ($\tau_C$) | 100 days | 100 days | 100 days | 80 days |
| Latency time ($\tau_L$) | 40 days | 40 days | 40 days | 160 days |
| Compressive strength ($f'_c$) | 38 MPa | 37 MPa | 34 MPa | 31 MPa |
| Tensile strength ($f'_t$) | 3.8 GPa | 3.7 MPa | 3.4 MPa | 3.1 MPa |
| $A_t$ coefficient for Mazars damage | 0.9 | 0.9 | 0.6 | 0.9 |
| $A_c$ coefficient for Mazars damage | 1.17 | 1.13 | 1.01 | 1.06 |
| $B_c$ coefficient for Mazars damage | 1500 | 1500 | 1500 | 1700 |
| Stress-free temperature | 23.0°C | 23.0°C | 23.0°C | 10.6°C |

Environmental temperature and moisture boundary conditions are applied on the outer surfaces of the beams as indicated in Figure 6 and Figure 7, respectively. Temperature and moisture were monitored inside the beams throughout the experimental period at multiple locations, as reported in[34]. Experimental observations for temperature and moisture inside the concrete bulk are missing for a period of time due to malfunctioning sensors. Temperature and moisture profiles at the sensor locations are compared between the simulations and experiments in Figure 6 and Figure 7, respectively. Temperature profiles from the simulations on both the outer surfaces and the bulk of the beams match with experimental observations. Moisture profiles for Beam 4 follow a drying trend similar to that observed in the experiment; however, there is an offset in the moisture values, which could be due to the overestimation of the moisture diffusion coefficient. The moisture profile from simulation in the concrete bulk for Beams 5 and 6 does not match the experimental observation. This discrepancy is believed to be due to sensor malfunctions, because the experimentally observed moisture value from the top sensor should be between the values from the ambient and middle sensors, which is not the case.

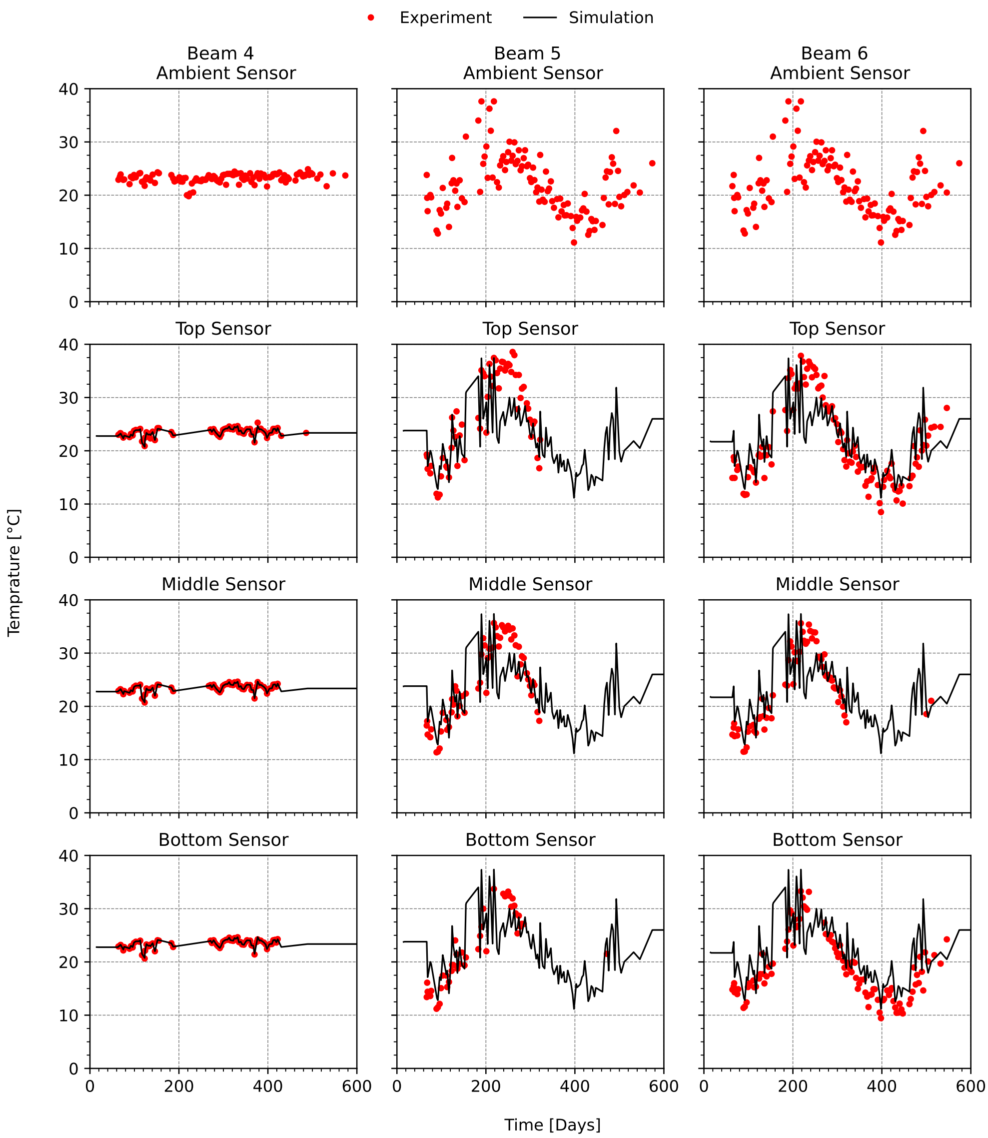


**Figure 6** Temperature histories at multiple locations for the USC beams, with comparisons between experimental data and simulation results.

Time histories of strains in the $x$ (axial) and $y$ (vertical) directions, which are primarily due to ASR, were obtained from the experiments at points at the middle of the shear spans and are compared with simulation results in Figure 8. Reported strains include contributions from all sources. Error bars in the figure represent one standard deviation in the experimental data. The simulations predicted the ASR expansion in both directions reasonably well for the duration of the experiments. Greater ASR expansion is observed in Beam 6 than in Beams 4 and 5, which is expected due to the presence of 1.25% NaOH to accelerate ASR in the concrete mix for Beam 6. The ASR expansion in the $y$-direction is observed to be greater compared to the $x$-direction,

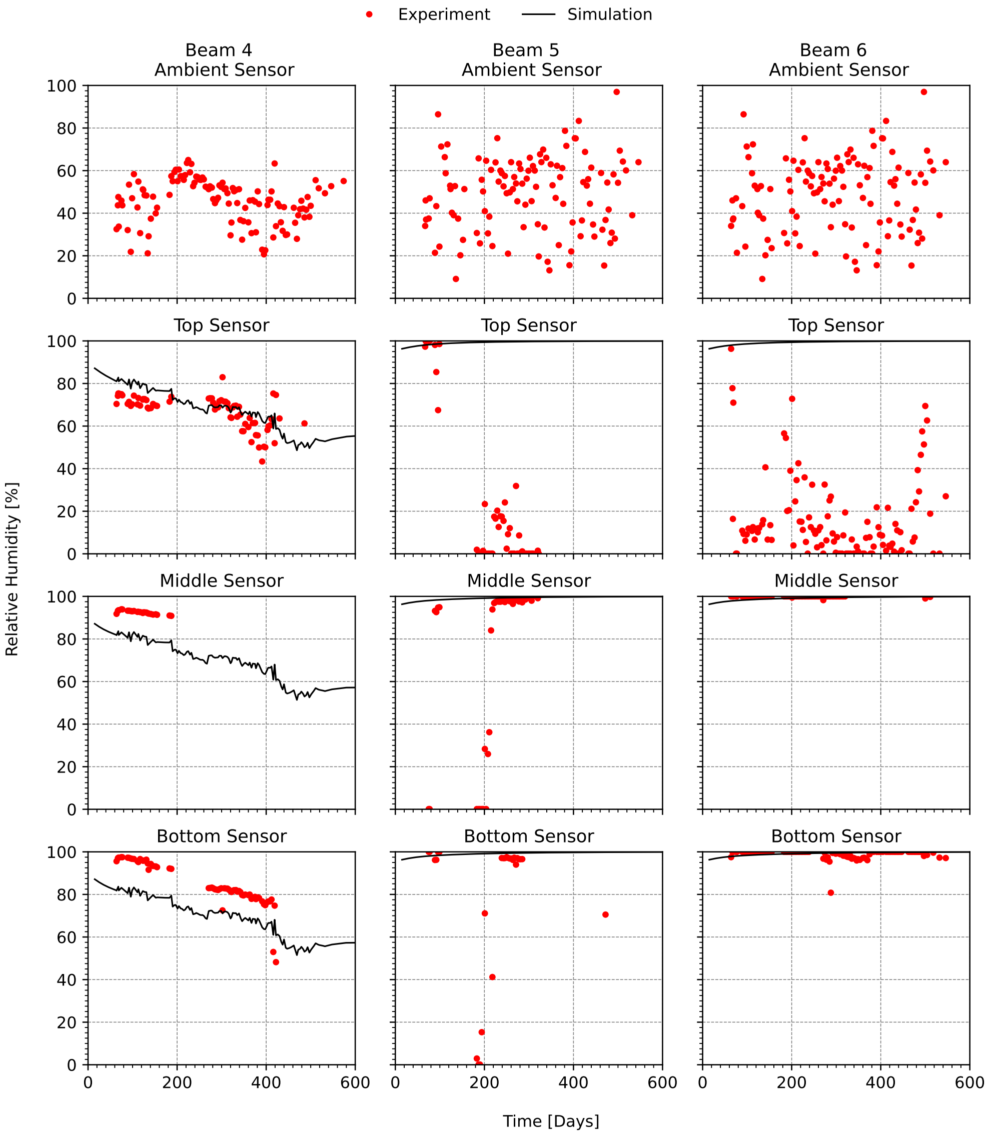


**Figure 7** Relative humidity histories for multiple locations for the USC beams, with comparisons between experimental data and simulation results.

which is due to higher confinement in the concrete bulk in the $x$-direction than the $y$-direction. The average volumetric ASR expansion from the simulations is compared in Figure 9 for the lightly and heavily confined regions in the beams. There are no experimental data for the middle span, where there is heavy confinement, but the observed behavior of greater expansion in the shear span is as expected due to the decreased confinement there.

### 4.2.2 | University of Texas beam

An RC beam tested at UT by Wald[35] was used here as another member-scale validation case. This beam had a 910 mm depth, 610 mm width, and 8,435 mm length and had the unique feature of only having biaxial reinforcement (longitudinal bars and vertical shear stirrups but no lateral reinforcement, except for stirrups at its ends). This arrangement is relevant for RC containments, which also are biaxially reinforced. Reactive cement and aggregate were used in the mix proportion to accelerate the ASR-induced expansion in the beam. The mix proportion of concrete and hardened concrete properties are described in detail in[35]. The beam was divided into three zones: A, B, and C, based on environmental conditions and reinforcement detailing. Zones

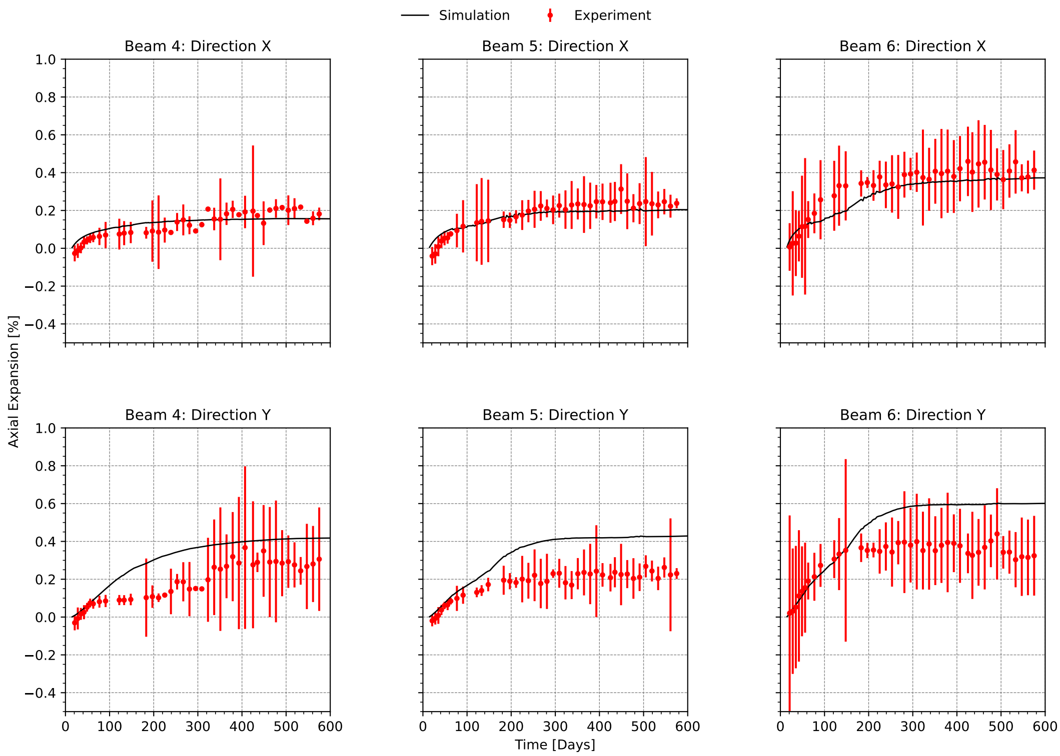


**Figure 8** Strain histories for the USC beams in the $x$- and $y$-directions (i.e. axial and vertical directions) at the middle of the shear span, with comparisons between experimental data and simulation results.

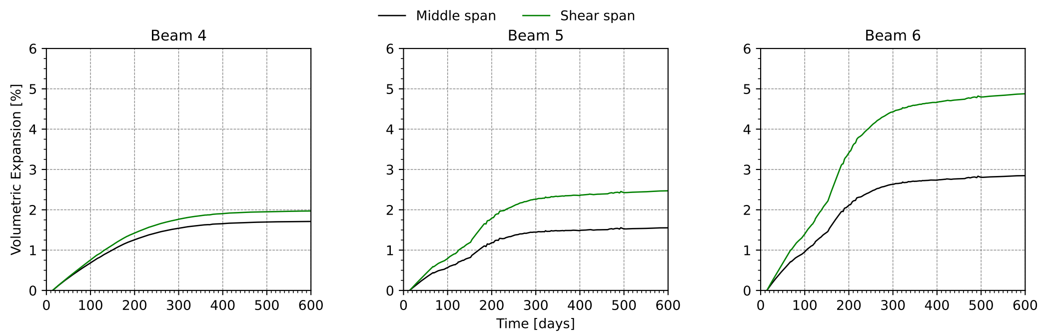


**Figure 9** Time histories of volume-averaged expansion from simulations of the USC beams comparing behavior in the middle span (high confinement) and shear span (light confinement).

A and B were periodically moistened, while Zone C was kept in constant wet conditions. Zone A was at the mid-span, away from the stirrups, while Zones B and C were at the ends of the beam, near the stirrups. The beam was stored in an outdoor environmental conditioning facility where the temperature was 5–10°C higher than the ambient temperature. The environmental temperature and moisture history are shown in Figure 10.

ASR expansion was monitored separately in each zone using calipers and vibrating wire gages. However, only readings from the caliper were used in the present validation effort, as they were the main data source in the experimental study. The measurements from the caliper provide four readings along the $x$ and $y$ directions and two readings along the $z$-direction. Reported strains include contributions from all sources. The three zones with varying environmental conditions and reinforcement detailing are shown in the finite element model of the beam in Figure 11. The beam is sliced in the $z$-direction to show the reinforcement

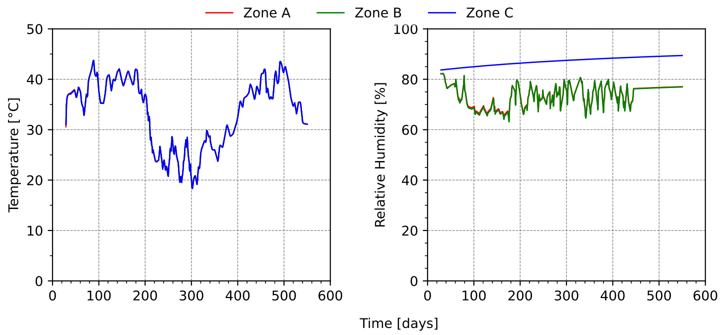


**Figure 10** Temperature and relative humidity histories recorded during the experiment for the UT beam during the testing period.

arrangement, which is symmetric about the $z$ plane. In the BlackBear model, the beam span is divided into four blocks corresponding to the ASR expansion measurement locations in Zones A, B, and C, and the rest of the span is assigned to the fourth block. The results from the fourth block are not used for comparison purposes as no experimental observations are available for that region. The modeling parameters for the beam are indicated in Table 4.

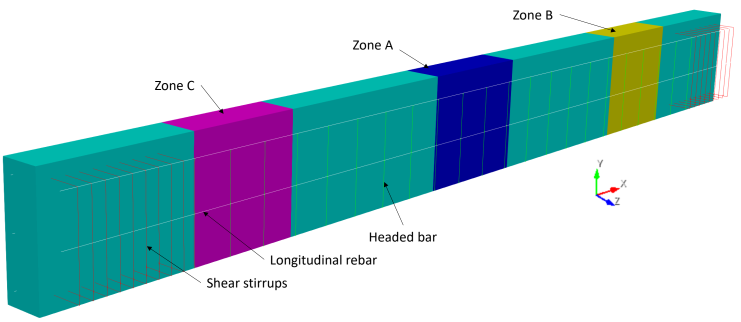


**Figure 11** Finite element model of UT RC beam, showing the zones with varying confinement and environmental conditions. The front half of the concrete is clipped by the $z$-plane to show the arrangement of rebar, modeled as truss elements.

The finite element model for this beam was set up in a manner similar to the USC beams, using properties defined in Table 4. Thermal boundary conditions were assumed to be spatially uniform over the entire beam; therefore, the temperature profile for all zones and the environmental temperature overlap, as shown in Figure 10. Relative humidity boundary conditions for Zones A and B are the same as the environmental relative humidity. For Zone C, relative humidity boundary conditions were assumed to be 95% for the entire experiment duration to represent wet conditioning in that region.

Volumetric ASR expansion from the simulation in the three zones are compared with the experimental results from[35] in Figure 12. The simulation predicts the ASR expansion reasonably well for the entire duration of the experiment. The simulation captures the effect of differences in the environmental boundary conditions on ASR expansion in Zones B and C. ASR expansion in Zones A and B are similar due to exposure to the same environmental conditions, while Zone C experiences greater ASR expansion, both in the simulation and experiments, due to the elevated humidity conditions it was exposed to. Differences in the response in Zones A and B due to proximity to the stirrups are minimal.

## 5 | SUMMARY AND CONCLUSIONS

A thermo-hygro-mechanical model for ASR-induced degradation in RC structures has been integrated into a modern, open-source, parallel computational framework, and validated against experimental data for RC specimens and members. This

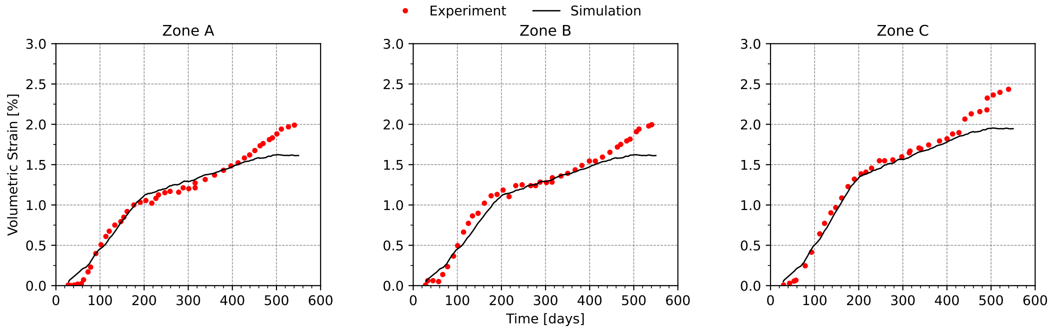


**Figure 12** Time histories of volumetric expansion in Zones A, B, and C of the UT beam, comparing simulation and experimental results.

numerical model simulates the ASR extent, expansion, and damage, which depend on the local temperature, moisture, confinement, and stress state. The primary focus in this study was on the free expansion of RC specimens and members due to ASR, with an emphasis on the confining effect of reinforcing bars.

For most of the validation cases considered, when the concrete ASR model is calibrated for similar environmental conditions as the RC experiments, model predictions closely match the experimental observations, especially in the early stages of ASR. However, in multiple cases considered here, the simulations tended to predict no further ASR expansion late in time after ASR has saturated, while the experiments often indicate low rates of continued expansion. The models used here follow the trend proposed by Larive[6], which flattens out after ASR is complete. Wallau et al.[57] showed that the ASR expansion model proposed by Mukhopadhyay and Liu[58] complies better with their experimental data. Such a model could be incorporated into the framework developed here and is a topic for further study. Furthermore, while multiple experiments were simulated here, this set of validation problems can be expanded to include a wider variety of conditions.

The validation cases considered here primarily test the model's ability to predict ASR-induced expansion under a variety of confining conditions. While the model employed here predicts damage and creep, both of which affect expansion, this aspect of the model has not been directly validated against experimental results in this paper. Related to this, the effects of ASR on structural capacity and ductility have also not been addressed here. Both of these are important topics for further validation studies.

## ACKNOWLEDGMENTS

This research was supported by multiple U.S. Department of Energy programs: the Office of Nuclear Energy's Light Water Reactor Sustainability and Nuclear Energy Advanced Modeling and Simulation programs, and the Office of Environment, Health, Safety and Security's Nuclear Safety Research and Development program, managed within the Office of Nuclear Safety. This research utilized the resources of the High Performance Computing Center at Idaho National Laboratory, which is supported by the Office of Nuclear Energy of the U.S. Department of Energy and the Nuclear Science User Facilities under contract no. DE-AC07-05ID14517. This manuscript was authored by Battelle Energy Alliance, LLC under contract no. DE-AC07-05ID14517 with the U.S. Department of Energy. The U.S. Government retains a nonexclusive, paid-up, irrevocable, worldwide license to publish or reproduce the published form of this manuscript, or allow others to do so, for U.S. Government purposes.

## References

1. Saouma V, and Perotti L. Constitutive Model for Alkali-Aggregate Reactions. ACI Materials Journal. 2006;**103**(3).
2. Dupuis R, and Pellenq RJM. Alkali silica reaction: A view from the nanoscale. Cement and Concrete Research. 2022;**152**:106652.

3. Ulm FJ, Coussy O, Kefei L, and Larive C. Thermo-Chemo-Mechanics of ASR Expansion in Concrete Structures. Journal of Engineering Mechanics. 2000 Mar;**126**(3):233–242.
4. Wei J, Gencturk B, Jain A, and Hanifehzadeh M. Mitigating alkali-silica reaction induced concrete degradation through cement substitution by metakaolin and bentonite. Applied Clay Science. 2019;**182**:105257.
5. Pathirage M, Zhang B, Alnaggar M, and Cusatis G. Confinement and alkali-silica reaction in concrete: Review and numerical investigation. International Journal of Solids and Structures. 2023 Aug;**277-278**:112341.
6. Larive C. Apports Combin'es de l'Experimentation et de la Modélisation à la Comprehension del' A lcali-Réaction et de ses Effets Mécaniques, (Ph.D. Thesis). Laboratoire Central des Ponts et Chaussées. Paris, France; 1998.
7. Multon S, and Toutlemonde F. Effect of applied stresses on alkali–silica reaction-induced expansions. Cement and Concrete Research. 2006;**36**(5):912–920.
8. Gautam BP, and Panesar DK. A new method of applying long-term multiaxial stresses in concrete specimens undergoing ASR, and their triaxial expansions. Materials and Structures. 2015 Oct;**49**(9):3495–3508.
9. Liaudat J, Carol I, López CM, and Saouma VE. ASR expansions in concrete under triaxial confinement. Cement and Concrete Composites. 2018 Feb;**86**:160–170.
10. Iskhakov T, Timothy JJ, and Meschke G. Expansion and deterioration of concrete due to ASR: Micromechanical modeling and analysis. Cement and Concrete Research. 2019;**115**:507–518.
11. Xi Y, Suwito A, Wen X, Meyer C, and Jin W. Testing and modeling alkali-silica reaction and the associated expansion of concrete. Mechanics of Quasi-Brittle Materials and Structures. In: Proceedings of International Workshop in honor of Prof ZP Bazant 60th birthday, Hermes Science Publications, Paris; 1998. .
12. Sellier A, and Capra B. Modélisation physico-chimique de la réaction alcali-granulat: apport au calcul des structures dégradées. Revue Française de Génie Civil. 1997 Jan;**1**(3):445–481.
13. Bažant ZP, and Steffens A. Mathematical model for kinetics of alkali–silica reaction in concrete. Cement and concrete research. 2000;**30**(3):419–428.
14. Multon S, Sellier A, and Cyr M. Chemo–mechanical modeling for prediction of alkali silica reaction (ASR) expansion. Cement and Concrete Research. 2009;**39**(6):490–500.
15. Esposito R, and Hendriks MAN. Literature review of modelling approaches for ASR in concrete: a new perspective. European Journal of Environmental and Civil Engineering. 2019;**23**(11):1311–1331.
16. Reinhardt HW, and Mielich O. A fracture mechanics approach to the crack formation in alkali-sensitive grains. Cement and Concrete Research. 2011;**41**(3):255–262.
17. Bažant ZP, Zi G, and Meyer C. Fracture mechanics of ASR in concretes with waste glass particles of different sizes. Journal of engineering mechanics. 2000;**126**(3):226–232.
18. Poyet S, Sellier A, Capra B, Foray G, Torrenti JM, Cognon H, et al. Chemical modelling of alkali silica reaction: Influence of the reactive aggregate size distribution. Materials and structures. 2007;**40**(2):229–239.
19. Suwito A, Jin W, Xi Y, and Meyer C. A mathematical model for the pessimum size effect of ASR in concrete. Concrete Science and Engineering. 2002;**4**(13):23–34.
20. Nguyen TDH, Maschietti M, Åmand LE, Vamling L, Olausson L, Andersson SI, et al. The effect of temperature on the catalytic conversion of Kraft lignin using near-critical water. Bioresource Technology. 2014;**170**:196–203.
21. Liaudat J, López CM, and Carol I. Diffusion-reaction model for ASR: formulation and 1D numerical implementation. Computational Modelling of Concrete and Concrete Structures. 2014;p. 639–648.
22. Léger P, Côté P, and Tinawi R. Finite element analysis of concrete swelling due to alkali-aggregate reactions in dams. Computers & Structures. 1996;**60**(4):601–611.

23. Capra B, and Bournazel JP. Modeling of induced mechanical effects of alkali-aggregate reactions. Cement and Concrete Research. 1998;**28**(2):251–260.

24. Winnicki A, and Pietruszczak S. On mechanical degradation of reinforced concrete affected by alkali-silica reaction. Journal of Engineering Mechanics. 2008;**134**(8):611–627.

25. Comi C, Fedele R, and Perego U. A chemo-thermo-damage model for the analysis of concrete dams affected by alkali-silica reaction. Mechanics of Materials. 2009 Mar;**41**(3):210–230.

26. Comi C, Kirchmayr B, and Pignatelli R. Two-phase damage modeling of concrete affected by alkali–silica reaction under variable temperature and humidity conditions. International Journal of Solids and Structures. 2012 Nov;**49**(23-24):3367–3380.

27. Ferche AC, Gautam B, Habibi F, Panesar DK, Sheikh SA, Vecchio FJ, et al. Material, structural and modelling aspects of alkali aggregate reaction in concrete. Nuclear Engineering and Design. 2019 Sep;**351**:87–93.

28. Gallyamov ER, Corrado M, Fauriel J, and Molinari JF. Long-term behaviour of a dam affected by alkali-silica reaction studied by a multi-scale model. Engineering Structures. 2023 Feb;**277**:115427.

29. Commission USNR. Special NRC Oversight at Seabrook Nuclear Power Plant: Concrete Degradation; 2012. Available from: https://www.nrc.gov/reactors/operating/ops-experience/concrete-degradation.html.

30. Manabe R, Kawae H, Ogawa K, and Matsuura M. Maintenance Management of Turbine Generator Foundation Affected by Alkali–Silica Reaction. Journal of Advanced Concrete Technology. 2016;**14**(9):590–606.

31. Saouma VE, and Hariri-Ardebili MA. Seismic capacity and fragility analysis of an ASR-affected nuclear containment vessel structure. Nuclear Engineering and Design. 2019;**346**:140–156.

32. Veeraraghavan S, Bolisetti C, Slaughter A, Coleman J, Dhulipala SLN, Hoffman W, et al. MASTODON: an open-source software for seismic analysis and risk assessment of critical infrastructure. Nuclear Technology. 2021;**207**(7):1073–1095.

33. Wald DM, Allford MT, Bayrak O, and Hrynyk TD. Development and multiaxial distribution of expansions in reinforced concrete elements affected by alkali–silica reaction. Structural Concrete. 2017;**18**:914–928. Available from: 10.1002/suco.201600220.

34. Ballarini R, Gencturk B, Jain A, Aryan H, Xi Y, Abdelrahman M, et al.. 2020. *Multiple Degradation Mechanisms in Reinforced Concrete Structures, Modeling and Risk Analysis*. INL/EXT-20-57095. Idaho National Laboratory.

35. Wald DM. ASR expansion behavior in reinforced concrete: experimentation and numerical modeling for practical application (Ph.D. Thesis). The University of Texas at Austin. Austin, Texas, USA; 2017. Available from: http://hdl.handle.net/2152/61820.

36. Multon S, Seignol JF, and Toutlemonde F. Structural behavior of concrete beams affected by alkali-silica reaction. ACI Materials Journal. 2005;**102**(2):67.

37. Karthik MM, Mander JB, and Hurlebaus S. Experimental behavior of large reinforced concrete specimen with heavy ASR and DEF deterioration. Journal of Structural Engineering. 2018;**144**(8):04018110.

38. Habibi F, Sheikh SA, Vecchio F, and Panesar DK. Effects of alkali-silica reaction on concrete squat shear walls. ACI Structural Journal. 2018;**115**(5):1329–1339.

39. Eurocode. 2004. *Design of concrete structures. Part 1-2: general rules - structural fire design*. . European Committee for Standardization, Brussels, Belgium.

40. Xi Y, Bažant ZP, Molina L, and Jennings HM. Moisture diffusion in cementitious materials Moisture capacity and diffusivity. Advanced Cement Based Materials. 1994 November;**1**(6):258–266.

41. Bary B, de Morais MVG, Poyet S, and Durand S. Simulations of the thermo-hydro-mechanical behaviour of an annular reinforced concrete structure heated up to 200°C. Engineering Structures. 2012 Mar;**36**:302–315.

42. Multon S. Experimental and theoretical evaluation of mechanical effects of alkali-silica reaction on laboratory structures (Ph.D. Thesis). Marne-la-Vallée. Paris, France; 2003.

43. Giorla A. 2017. *Implementation of Concrete Creep Model in Grizzly*. ORNL/TM-2017/729. Oak Ridge, TN: Oak Ridge National Laboratory.

44. Mazars J. Application de la mécanique de l'endommagement au comportement non linéaire et à la rupture du béton de structure (Ph.D. Thesis). Université Paris 6. Paris, France; 1984.

45. Pijaudier-Cabot G, and Mazars J. Damage Models for Concrete. In: Lemaitre J, editor. Handbook of Materials Behavior Models. Academic Press; 2001. .

46. Spencer BW, Hoffman WM, Biswas S, Jiang W, Giorla A, and Backman MA. Grizzly and BlackBear: Structural Component Aging Simulation Codes. Nuclear Technology. 2021;**207**(7):981–1003.

47. et al ADL. 2.0 - MOOSE: Enabling massively parallel multiphysics simulation. SoftwareX. 2022 Dec;**20**:101202.

48. Kirk BS, Peterson JW, Stogner RH, and Carey GF. `libMesh`: A C++ Library for Parallel Adaptive Mesh Refinement/-Coarsening Simulations. Engineering with Computers. 2006;**22**(3–4):237–254.

49. Balay S, Gropp WD, McInnes LC, and Smith BF. Efficient Management of Parallelism in Object Oriented Numerical Software Libraries. In: Arge E, Bruaset AM, and Langtangen HP, editors. Modern Software Tools in Scientific Computing. Birkhäuser Press; 1997. p. 163–202.

50. Cheniour A, Davidson E, Pape YL, Pandya T, Collins B, Spencer B, et al. A Structural Model of the Long-term Degradation of the Concrete Biological Shield. Nuclear Engineering and Design. 2023 Apr;**405**:112217.

51. BlackBear source code repository; 2023. Available from: https://github.com/idaholab/blackbear.

52. MOOSE source code repository; 2023. Available from: https://github.com/idaholab/moose.

53. Huang H, Spencer BW, and Cai G. 2015. *Grizzly Model of Multi-Species Reactive Diffusion, Moisture/Heat Transfer and Alkali-Silica Reaction in Concrete*. INL/EXT-15-36425. Idaho Falls, ID: Idaho National Laboratory.

54. Spencer BW, and Huang H. Coupled Physics Simulation of Expansive Reactions in Concrete with the Grizzly Code. In: Jackson JH, Paraventi D, and Wright M, editors. Proceedings of the 18th International Conference on Environmental Degradation of Materials in Nuclear Power Systems - Water Reactors. Springer; 2017. p. 131–141.

55. Allford MT. Expansion Behavior of Reinforced Concrete Elements Due to Alkali-Silica Reaction (Masters Thesis). University of Texas, Austin; 2016. Available from: http://hdl.handle.net/2152/41645.

56. Gencturk B, Aryan H, Hanifehzadeh M, Chambreuil C, and Wei J. A Computational Study of the Shear Behavior of Reinforced Concrete Beams Affected from Alkali–Silica Reactivity Damage. Materials. 2021 Jun;**14**(12):3346.

57. Wallau W, Pirskawetz S, Voland K, and Meng B. Continuous expansion measurement in accelerated concrete prism testing for verifying ASR-expansion models. Materials and Structures. 2018 Jun;**51**(3).

58. Liu KW, and Mukhopadhyay AK. A kinetic-based ASR aggregate classification system. Construction and Building Materials. 2014;**68**(525).

59. Nielsen A, Gottfredsen F, and Thøgersen F. Development of stresses in concrete structures with alkali-silica reactions. Materials and structures. 1993;**26**(3):152–158.

60. Chénier JO, Komljenovic D, Gocevski V, Picard S, and Chrétien Gea. An approach regarding aging management program for concrete containment structure at the Gentilly-2 nuclear power plant. In: Proceedings of 33rd Annual Conference of the Canadian Nuclear Society, TCU Place, Saskatoon, Saskatchewan, Canada. vol. 1013; 2012. p. 126.

61. Lagerblad B, and Trágardh J. Slowly reacting aggregates in Sweden - Mechanism and conditions for reactivity in concrete. In: Proceedings of 33rd Annual Conference of the Canadian Nuclear Society, TCU Place, Saskatoon, Saskatchewan, Canada. vol. 1013; 2012. p. 126.

62. Fiset M, Sanchez LFM, Bilodeau S, Mitchell D, and Bastien J. Influence of Alkali-Silica reaction (ASR) on aggregate interlock and shear-friction behavior of reinforced concrete members. Engineering Structures. 2021;**233**:111890.

63. Aryan H, and Gencturk B. Influence of alkali-silica reaction on the shear capacity of reinforced concrete beams with minimum transverse reinforcement. Engineering Structures. 2021;**235**:112020.

64. Morenon P, Multon S, Sellier A, Grimal E, Hamon F, and Kolmayer P. Flexural performance of reinforced concrete beams damaged by Alkali-Silica Reaction. Cement and Concrete Composites. 2019;**104**:103412.

65. Sawada S, Takaine Y, Okayasu T, Nimura A, and Shimamoto R. Structural Performance Evaluation and Monitoring of Reinforced Concrete Shear Walls Affected by Alkali-Silica Reactions. Journal of Advanced Concrete Technology. 2021;**19**(5):477–500.

66. Sellier A, and Capra B. Physico-chemical mod ’e lization of the alkali-aggregate reaction: contribution to the calculation of the structures of é grad ’e es. Revue fran c c aise de g ’e nie civil. 1997;**1**(3):445–481.

67. Multon S, Merliot E, Joly M, and Toutlemonde F. Water distribution in beams damaged by alkali-silica reaction: global weighing and local gammadensitometry. Materials and Structures. 2004;**37**(5):282–288.

68. ASCE. 1992. *Structural Fire Protection, ASCE Committee on Fire Protection, Structural Division*. . New York, NY, USA: American Society of Civil Engineers.

69. Bell JE, Palecki MA, Baker CB, Collins WG, Lawrimore JH, Leeper RD, et al. U.S. Climate Reference Network Soil Moisture and Temperature Observations. Journal of Hydrometeorology. 2013;**14**(3):977 – 988.

70. Armson D, Stringer P, and Ennos AR. The effect of tree shade and grass on surface and globe temperatures in an urban area. Urban Forestry & Urban Greening. 2012;**11**(3):245–255.

71. Clauss DB. 1987. *Round-Robin Pretest Analyses of a 1:6-Scale Reinforced Concrete Containment Model Subject to Static Internal Pressurization*. NUREG/CR-4913, SAND87-0891. Albuquerque, NM: Sandia National Laboratories.

72. Kodur VKR, Wang TC, and Cheng FP. Predicting the fire resistance behaviour of high strength concrete columns. Cement and Concrete Composites. 2004;**26**(2):141–153.

73. Wittmann FH, Rokugo K, Brühwiler E, Mihashi H, and Simonin P. Fracture energy and strain softening of concrete as determined by means of compact tension specimens. Materials and Structures. 1988;**21**(1):21–32.

74. Wilkins A, Spencer BW, Jain A, and Gencturk B. A method for smoothing multiple yield functions. International Journal for Numerical Methods in Engineering. 2020;**121**(3):434–449.


□